Universidad de La Laguna

Facultad de Ciencias

BSc in Physics

2024-25 course

BSc Thesis

Photometric analysis of the eclipsing binary system ASASSN-V J050229.84-052203.4

Author:
Elena Ruiz Laguna

Supervisor:
María Jesús Arévalo Morales
Departamento de Astrofísica, Universidad de La Laguna
Instituto de Astrofísica de Canarias

Co-supervisor:
Daniel Galán Diéguez
Departamento de Astrofísica, Universidad de La Laguna
Instituto de Astrofísica de Canarias

June 2025

Facultad de Ciencias
BSc in Astrophysics
2024-25 course
BSc Thesis

Photometric analysis of the eclipsing binary system ASASSN-V J050229.84-052203.4

Author: **Elena Ruiz Laguna**
Departamento de Astrofísica, Universidad de La Laguna
alu0101441917@ull.edu.es

Supervisor: **María Jesús Arévalo Morales**,
Departamento de Astrofísica, Universidad de La Laguna
Instituto de Astrofísica de Canarias
mam@iac.es

Co-supervisor: **Daniel Galán Diéguez**,
Departamento de Astrofísica, Universidad de La Laguna
Instituto de Astrofísica de Canarias
daniel.galan@iac.es

A mamá, por impulsar mis sueños aunque supusieran tener que estar a 1600 km la una de la otra. A papá, por compartir conmigo esta pasión por la ciencia. A mis hermanas, Alba y María, porque fueron, son y serán mis compañeras de vida. A Juan, por haberme acompañado en este camino a pesar de las adversidades. A los amigos que hice en el grado, porque juntos hemos luchado hasta llegar aquí. En especial a Zenaida y Miguel, porque no solo me tenían que aguantar en la facultad, sino también en casa. A Rafa G. Farfán, ese profesor que me abrió las puertas al mundo de la astrofísica y me inculcó el amor a ella. Y por supuesto, a María Jesús y Daniel, mis tutores, por haber sacado siempre tiempo, ganas y paciencia para mí. En resumen, gracias a todos los que creyeron en mí cuando ni yo misma lo hacía.

"¿Había algo mejor en la vida que buscar respuestas?" - Isaac Asimov

Resumen

Contexto. La mayoría de las estrellas no se forman solas, sino en sistemas binarios o múltiples, siendo estos últimos los más abundantes en el universo. Dentro de ellos, los sistemas binarios eclipsantes son especialmente valiosos, ya que son los únicos que permiten determinar de forma precisa parámetros físicos como la razón de radios, gracias a las curvas de luz fotométricas, la relación de temperaturas por curvas de luz observadas en distintos filtros, y las masas por medidas espectroscópicas que permiten obtener las curvas de velocidad radial.

Objetivos. El objetivo de este trabajo es realizar el análisis fotométrico del sistema binario eclipsante ASASSN-V J050229.84-052203.4. A partir de dicho análisis se obtienen una nueva curva de luz (mejor muestrada que la existente en la literatura), los parámetros físicos, sus magnitudes calibradas y los colores del sistema binario.

Métodos. Para el estudio fotométrico de la binaria ASASSN-V J050229.84-052203.4 se hicieron observaciones en el telescopio IAC80 del Observatorio del Teide. La reducción y tratamiento de los datos obtenidos se realiza con una serie de programas desarrollados en Python por mi cotutor, Daniel Galán; con ellos se lleva a cabo la fotometría diferencial y se obtienen las curvas de luz del sistema binario eclipsante. Además, para la calibración fotométrica en los filtros Johnson V, R e I, se usa un programa en IDL desarrollado por el Dr. Ramón Iglesias Marzoa. Finalmente, las curvas de luz se ajustan con los software para modelado de binarias eclipsantes `PHOEBE2` y `BinaRoche` que nos proporcionan medidas independientes de los parámetros fisicos de las componentes del sistema binario.

Resultados. Se obtienen resultados para los parámetros físicos del sistema binario eclipsante ASASSN-V J050229.84-052203.4. Asumiendo una órbita circular, la temperatura efectiva para la componente primaria es apoximadamente $T_{eff,1} = 8000\,K$, y teniendo en cuenta el ratio entre temperaturas, la temperatura para la componente secundaria se aproxima a $T_{eff,2} = 4760\,K$. Además, se obtuvo un ratio de masas fotométricas de $q = 0.3698$, un ratio de radios $k = 0.8861$ y una inclinación para la órbita de $i = 80°$.

En el caso de los tipos espectrales, la componente primaria es una estrella tipo A. Para la secundaria, sin embargo, no fue posible determinar con precisión sus colores ya que en el eclipse primario existe aún contribución de flujo de la estrella primaria. Sin embargo, atendiendo al ratio de masas y a las temperaturas efectivas, estimamos que esté entre una estrella de tipo espectral K2 y K5.

Contents

1 Introduction

Resumen: En este capítulo se introducen los sistemas binarios, enfocándonos en los eclipsantes, donde una estrella oculta a la otra desde nuestra perspectiva, provocando variaciones de brillo. Se explican los parámetros necesarios para describir estos sistemas, cómo se obtiene su curva de luz y la importancia de las curvas de velocidad radial para calcular masas y radios. También se presentan los tres tipos principales de binarias eclipsantes según su curva de luz: Algol, Beta Lyrae y W Ursae Majoris.

1.1 Binary stars

Binary stars are systems composed of two stars that are bound by gravity and orbiting a common center of mass (see Figure 1). Their existence has been proposed and discussed for a long time (Hernández et al., 2024). The first recorded observation of a binary star was Mizar, detected in 1650 by the astronomer Giovanni Battista Riccioli. At that time, most of these systems were discovered visually and identified as double stars (known now as visually binaries). It was not until 1802 when William Herschel formally introduced the term binary star. Nowadays, it is known that more than ~ 80% of the stars are part of binary or multiple systems (Alonzo-Carrillo, 2015).

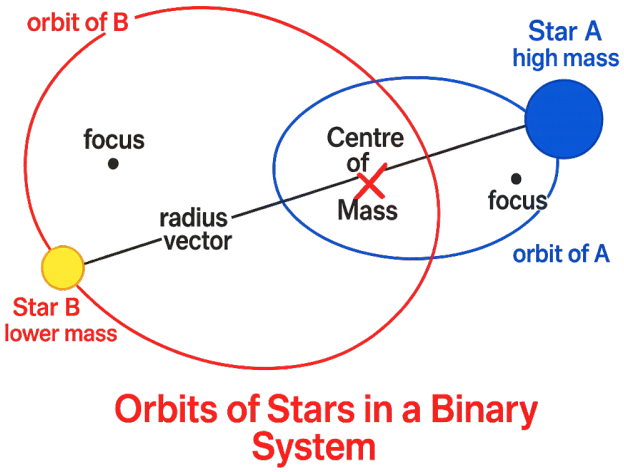

Figure 1: Geometric scheme of binary stars (Tawalbeh and Al-Wardat, 2018)

As it can be seen throughout this work, the study of these systems provides crucial information for understanding stellar evolution, since both stars in a binary system form at the same time and evolve together. Although there are several types of binary stars, this work will focus on the study of eclipsing binary systems.

1.2 Eclipsing binaries

In 1783, John Goodricke was the first to invoke the concept of stellar eclipses, in order to explain the light variations in β Persei (Southworth, 2012). Eclipsing binaries are those systems in which the orbital plane of the system is almost side on as seen from Earth; so that, as the stars move around a common center of gravity, passing one in front of the other, they produce variations in brightness known as eclipses (British Astronomical Association, Variable Star Section, 2011).

The light curve of an eclipsing binary typically shows intervals of constant brightness interrupted by periodic, pronounced dips in brightness (e.g. eclipses, corresponding to one star passing in front of the other, see Figure 2). Throughout the orbit, the brightness may decrease twice, once when the secondary star eclipses the primary (primary eclipse), and again when the primary star obscure the secondary (secondary star) (Chen, 2024).

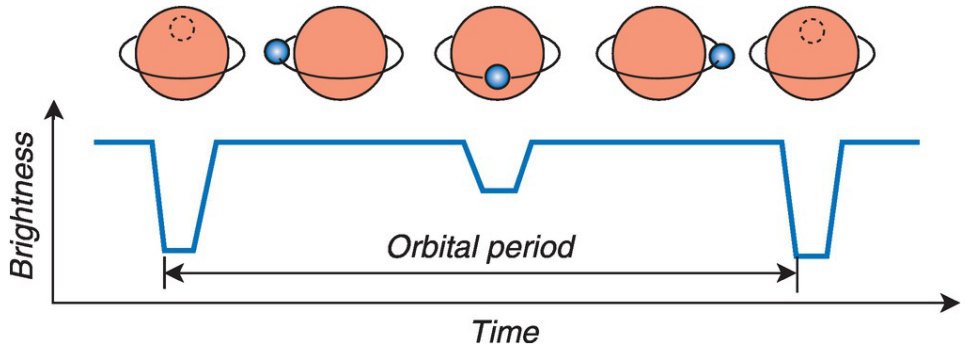

Figure 2: Light curve example of an eclipsing binary system (Christian and Roy, 2017)

1.3 Orbital parameters of eclipsing binary systems

For a complete description of an eclipsing binary, it is necessary to know 13 parameters, with 7 of them being orbital ones. These are period (P), orbital inclination (i), longitude os the ascending node (Ω), the argument of the periastron (ω), the semi-major axis (a), the eccentricity (e), and the time of a primary minimum (T_0), that should be given in Julian date (Taff, 1985 & Martínez-País, 2003). Some of them are shown in Figure 3.

The orbital inclination has a minimum value in order to see eclipses, i_m. If it is assumed that the orbit is circular (i.e. $e \approx 0$), a is the semi-major axis, and R_1 and R_2 the radii of the stars, then:

$$\mathrm{R_1 = x \cos i_m} \qquad \mathrm{R_2 = (a - x) \cos i_m} \tag{1}$$

Combining the previous expressions:

$$\cos \mathrm{i_m} = \frac{\mathrm{R_1 + R_2}}{\mathrm{a}} \tag{2}$$

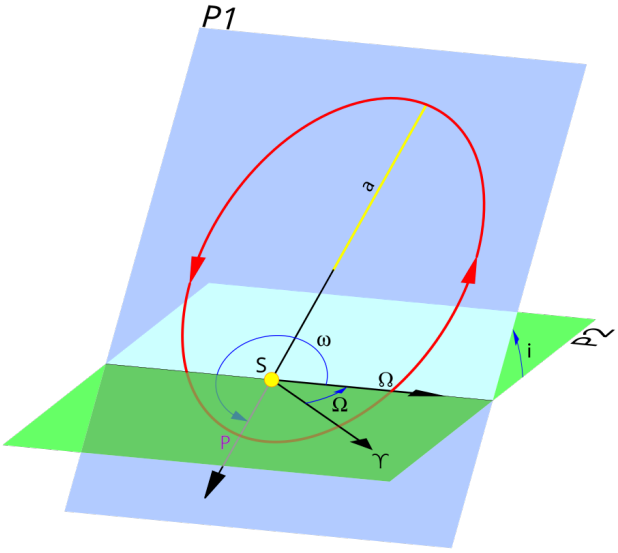

Figure 3: Schematics of an orbit showing its parameters by Brandir is licensed under CC BY-SA 3.0

1.4 Light curves of eclipsing binaries

To obtain a light curve, the first step is to compute the orbital phase, ϕ. This parameter ranges from 0 to 1, with the primary eclipse occurring at phases 0 and 1. The secondary eclipse will occur in a phase between 0 and 1, depending on the eccentricity of the orbit. But, if the orbit is circular ($e \approx 0$), the orbital phase for the secondary eclipse is $\phi = 0.5$. The phase is computed with the Julian date of the observation, using that:

$$\begin{cases} z = \frac{HJD - HJD_0}{P} \\ \\ \phi = z - [z] \end{cases} \tag{3}$$

where HJD is the Heliocentric Julian Date, HJD_0 the ephemeris origin in HJD, P the orbital period and [z] the integer part of z.

To obtain a light curve, we plot the relative flux (flux of the binary system compared with the flux of the comparison star) or differential magnitude (difference between the magnitude of a comparison star, that is not variable, and the magnitude of the binary system) against the orbital phases (see Figure 2).

Once we have the light curve, we can model it to estimate parameters like e, ω, i, effective temperatures (T_{eff}) or luminosities (L). Using both light and radial velocity curves (obtained with spectra at different orbital phases, see Section 1.5), we can determine also the masses and radii of both components.

1.5 Radial velocity curves

As we mentioned before, to obtain masses and radii of the binary system components, it is necessary to have radial velocity curves.

Because orbital motion, the stellar components move toward or away from us, causing their spec-

tral lines shift back and forth (blue- or red-shift) due to the Doppler effect (positions 1 and 3 in Figure 4). In contrast, when the components do not have orbital velocity relative to the observer (positions 2 and 4 in Figure 4), the spectral lines do not shift. Using the Doppler equation, the radial velocities of the system (v_r) can be computed; in each phase, with a shift of spectral lines $\Delta\lambda$ respect to its stationary position λ the $v_r(\phi)$ is:

$$v_r(\phi) = \frac{\Delta\lambda}{\lambda} c \tag{4}$$

with c the speed of light in vacuum. Representing $v_r(t)$ against time, one can obtain radial velocity curves.

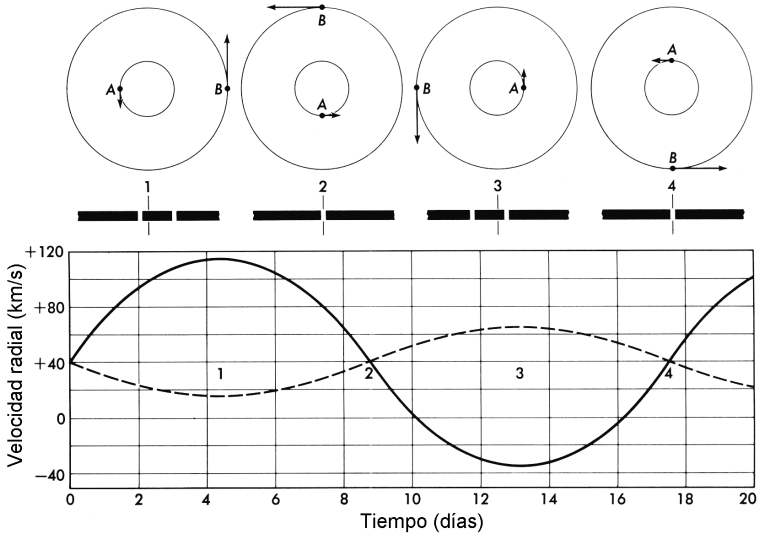

Figure 4: Radial velocity curves of a hypothetical spectroscopic binary with circular orbits (Vives, 2003).

Taking into account that the position of the center of masses is given by

$$\overrightarrow{r_{cm}} = \frac{M_1\overrightarrow{r_1} + M_2\overrightarrow{r_2}}{M_1 + M_2}, \tag{5}$$

with M_i the masses of the components and $\overrightarrow{r_{cm}}$ the position of the components, if we put the reference system in that point, i.e., $\overrightarrow{r_{cm}} = 0$, then:

$$M_1\overrightarrow{r_1} + M_2\overrightarrow{r_2} = 0 \tag{6}$$

$$M_1\overrightarrow{r_1} = -M_2\overrightarrow{r_2} \rightarrow M_1|\overrightarrow{r_1}| = M_2|\overrightarrow{r_2}| \rightarrow \frac{M_1}{M_2} = \frac{|\overrightarrow{r_2}|}{|\overrightarrow{r_1}|} \tag{7}$$

Also:

$$|\overrightarrow{r}| = \frac{a(1-e^2)}{1 + e\cos\nu} \quad ; \quad \text{if } e = 0 \rightarrow |\overrightarrow{r}| = a \tag{8}$$

where e is the eccentricity and ν is the true anomaly, a parameter that represents the angle subtending the segments from the barycenter to the periastron and from the barycenter to the celestial body. Then, from Equation 7 and Equation 8:

$$\frac{M_1}{M_2} = \frac{a_2}{a_1} \tag{9}$$

We define the radial velocity semi-amplitudes as:

$$\begin{cases} K_1 = a_1 \sin i \\ K_2 = a_2 \sin i \end{cases} \tag{10}$$

where $K = K_1 + K_2$. Using Equation 9:

$$\frac{M_1}{M_2} = \frac{a_2}{a_1}\frac{\sin i}{\sin i} = \frac{K_2}{K_1} \tag{11}$$

From Perryman, 2018, the radial velocity semi-amplitudes fulfill:

$$\begin{cases} K_1^2 = \frac{G}{a_1 \sin i}\frac{P^2}{4\pi^2}\frac{M_2^3 \sin^3 i}{(M_1+M_2)^2} \\ K_2^2 = \frac{G}{a_2 \sin i}\frac{P^2}{4\pi^2}\frac{M_1^3 \sin^3 i}{(M_1+M_2)^2} \end{cases} \tag{12}$$

Taking into account Equation 10 and Equation 12:

$$\begin{cases} M_1 = \frac{4\pi^2 K_2 K^2}{P^2 G \sin^3 i} \\ M_2 = \frac{4\pi^2 K_1 K^2}{P^2 G \sin^3 i} \end{cases} \tag{13}$$

So, if we know the radial velocity semi-amplitudes, the orbital period and the orbital inclination, we can obtain the masses of both components.

1.6 Types of eclipsing binaries according to its light curve

1.6.1 EA Systems - Algol type

Algol systems are a class of eclipsing binaries characterized by light curves showing minimal variations outside the eclipses. In this systems, the stars are generally spherical and detached (see Figure 5 British Astronomical Association, Variable Star Section, 2011).

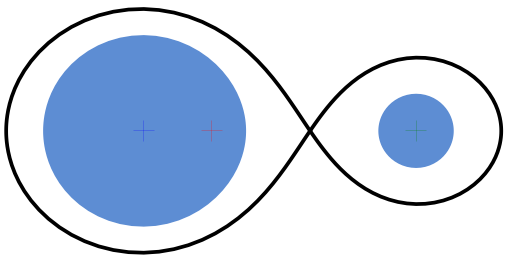

Figure 5: Detached binary star system, by Philip D. Hall - Own work, CC BY-SA 4.0

The key feature of Algol type variable stars (compared to other eclipsing binaries) is the presence of well-defined primary and secondary minima in their light curves. This indicates that the components are not in contact and are not significantly deformed by mutual gravitational forces. Their light curves exhibit sharp, abrupt changes (see Figure 6), which allow for the precise determination of orbital periods ranging from fractions of a day to several years (Chen, 2024).

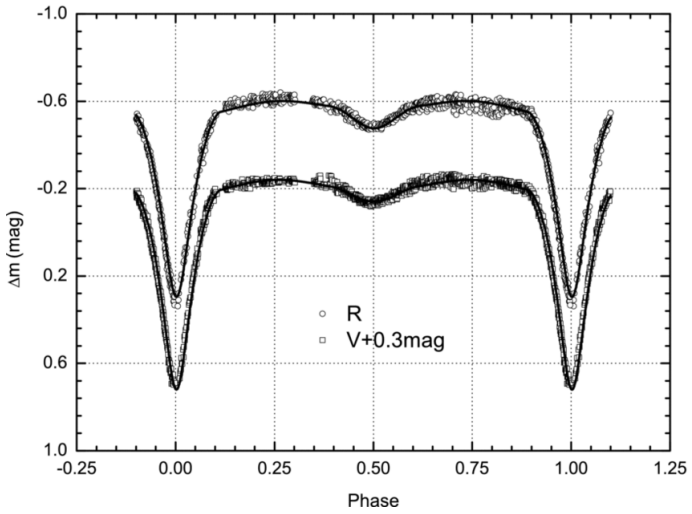

Figure 6: Light curves of the Algol-type eclipsing binary RV Trianguli in different photometric bands (Yang and Wei, 2008).

1.6.2 EB Systems - Beta Lyrae type

These systems consist of stars that are close enough to significantly distort each other through mutual gravitational interaction, resulting in ellipsoidal rather than spherical shapes (British Astronomical Association, Variable Star Section, 2011).

Despite their ellipsoidal geometry, Beta Lyrae stars still exhibit primary and secondary minima in their light curves. However, the transitions are smooth and gradual, making it difficult to determine the exact onset and end of the eclipses. This smoothness is primarily caused by substantial mass transfer between the components, which produces a shared envelope (i.e., common atmosphere), forming a semi-detached system (see Figure 7).

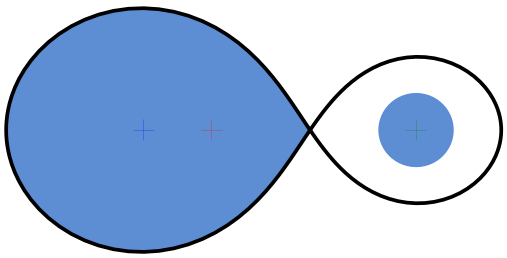

Figure 7: Semi-detached binary star system, by Philip D. Hall - Own work, CC BY-SA 4.0

The brightness variations of Beta Lyrae-type systems follow a regular and predictable pattern governed by their orbital periods, which typically span only a few days. The light curves of Beta Lyrae systems lack the sharp ingress and egress characteristic of Algol-type eclipses (see Figure 8). While sometimes classified as a subtype of Algol variables, Beta Lyrae systems are distinct in both their structure and light curve features (Chen, 2024).

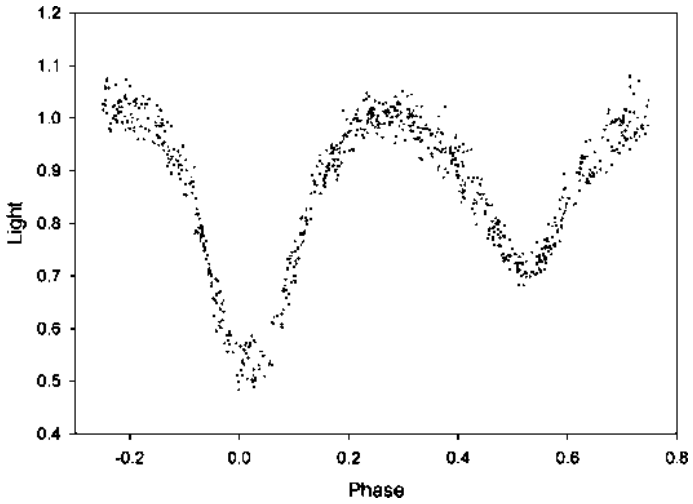

Figure 8: V band light curve of β Lyrae (Terrell, 2001)

1.6.3 EW Systems - W Ursae Majoris type

Contact binary stars consist of two stellar components so close that they share a common envelope, forming a continuous layer of matter between them (see Figure 9). Over time, their close proximity and ongoing mass exchange may lead to the eventual merger of the two stars into a single object. Although eclipses still occur and cause variations in brightness, the observed brightness fluctuations are subtle and symmetrical (both stars have similar surface temperatures and are heavily deformed by mutual gravitational forces, Chen, 2024). As shown in Figure 10, contact binaries do not exhibit sharply defined eclipses.

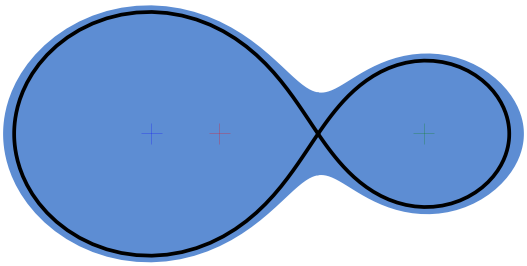

Figure 9: Contact binary star system, by Philip D. Hall - Own work, CC BY-SA 4.0

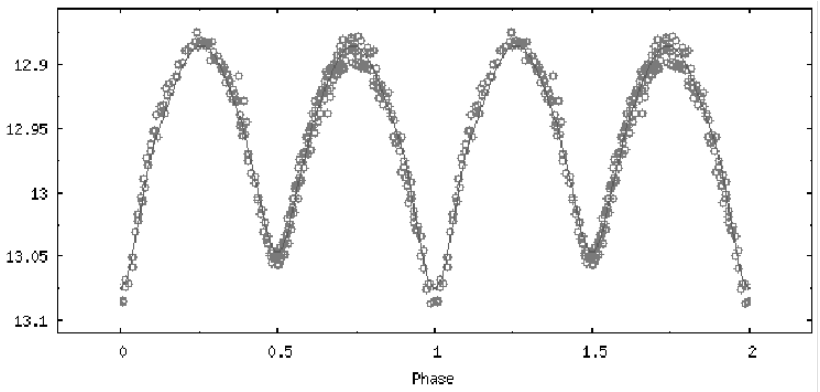

Figure 10: Light curve of the binary star system GSC 05765-01271 (Marullo et al., 2017)

2 Methods

Resumen: En este capítulo se describe el proceso seguido para el análisis fotométrico de la estrella binaria eclipsante ASASSN-V J050229.84-052203.4. Se seleccionó este sistema por su corto período orbital y su buena visibilidad desde Canarias. Las observaciones se realizaron con el telescopio IAC80 y la cámara CAMELOT2, aplicando técnicas como el autoguiado, la calibración con imágenes bias y flat-field, y la determinación de tiempos de exposición. Posteriormente, se procesaron los datos con los scripts `PhotoRed` (reducción), `AstroNet` (astrometría) y `BinaPhot` (fotometría diferencial). Se obtuvo la curva de luz a partir de mediciones precisas, comparando con estrellas de referencia y corrigiendo por efectos instrumentales y atmosféricos.

2.1 Object selection

ASASSN-V J050229.84-052203.4 (also known as CRTS J050229.7-052203, hereafter ASASSN-V) is an eclipsing binary listed in the ASAS-SN Variable Star Catalog as an EA variable star, as mentioned in the paper (Jayasinghe et al., 2018). This system is a strong candidate for further study due to several key factors: (i) it is a well-separated binary system with a short orbital period, which facilitates efficient sampling; (ii) its magnitude is well-suited for photometric observations using telescopes in the Canary Islands; and, (iii) the system was visible during the execution of this study, allowing direct observation (see Table 1).

Also, in 2023, Gareb Enoc Fernández Rodríguez did his BSc thesis about this binary system, where light curve modeling and stellar and orbital parameters determination were carried out (Fernández-Rodríguez, 2023). A portion of the light curve previously obtain by him was available, providing a good starting point for completing the curve and refining parameters. However, due to poor weather conditions, the light curves he obtained are not well sampled.

Table 1: ASASSN-V binary star system data. Coordinates and distance from Gaia Collaboration, 2020, period and epoch from Fernández-Rodríguez, 2023, and calibrated V magnitude from Drake et al., 2014.

Binary star system	ASASSN-V J050229.84-052203.4
α **(J2000)**	05:02:29.833
δ **(J200)**	-05:22:04.40
Distance [pc]	1298
Period [d]	0.7672625
Epoch [HJD]	2457359.86888
Calibrated V magnitude	13.81

2.2 Observation preparation and time assignment

We conducted the observations using the IAC80 telescope at the *Observatorio del Teide*. We chose this telescope due to the availability of observation time and the possibility to go to the telescope to gain experience with its operation. This telescope features an equatorial German mount, an effective focal ratio of $f/11.3$, an effective focal length of 9.02 m, and a primary mirror with a diameter of 82 cm (IAC, 2024d).

After selecting the binary system, we used the `BinarAlt` program, a script in the `PHOTOBIN` package developed by D. Galán Diéguez, designed to organize the observations. This program requires the user two .json files with specific information about the observatory and the celestial coordinates. Two key factors are essential in `BinarAlt`: the date and the location of the telescope (IAC, 2024d). Also, the IAC80 has a limitation in observation, with a 30º limit above the horizon; this restriction is structural because, if the telescope is positioned below 30º, mechanical stress on the mirrors occurs, requiring recalibration. This fact is taken in account in `BinarAlt`. Finally, the script produces two plots: one showing the visibility plot, and another indicating the observed phases during the observation nights (see Figure 11).

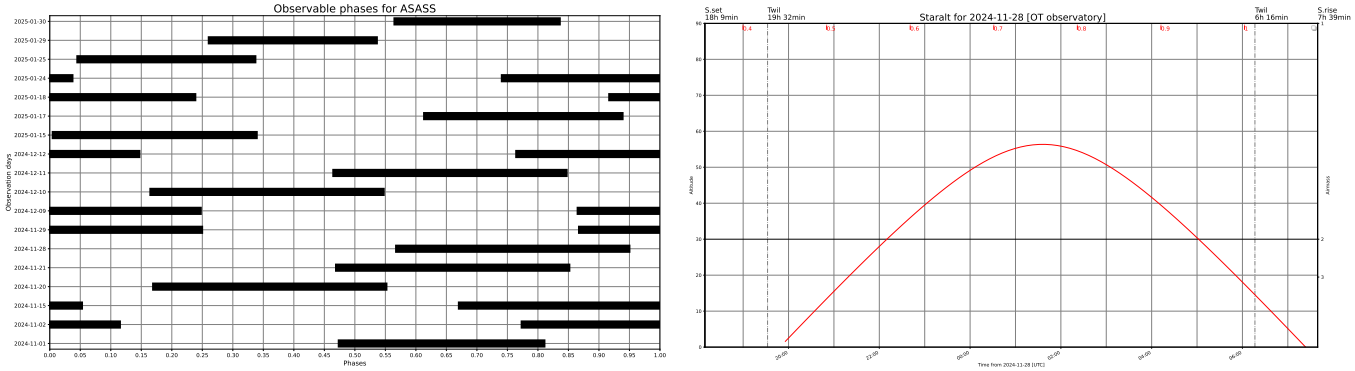

Figure 11: Output files from `BinarAlt`. Left: Observable phases during each observation night. Right: ASASN-V visibility plot (elevation) during a observation night.

We considered several factors when preparing the observation proposal. First, we used `BinarAlt` to select specific nights that would cover all phases of the binary system. Second, we selected comparison stars for conducting differential photometry. They should be within the telescope's field of view (FOV) and close to the binary system, with a similar brightness to prevent saturation during measurements. The ones selected for this work are shown in Figure 12. Also, we estimated exposure times using the exposure time calculator (IAC, 2024b).

The IAC Time Allocation Commission granted us with observing time after submitting a proposal detailing this project through the designated form. In total, we received 18 nights, spanning from early November to late January.

We organized the observing nights as follows: first, we took calibration images (bias and flat-fields images) before and during evening twilight (see Section 2.3.2 , where bias and flat-fields are discussed). Next, we observed the object during its visibility hours. Finally, when the system was not visible and if the night was photometric, we measured calibration stars.

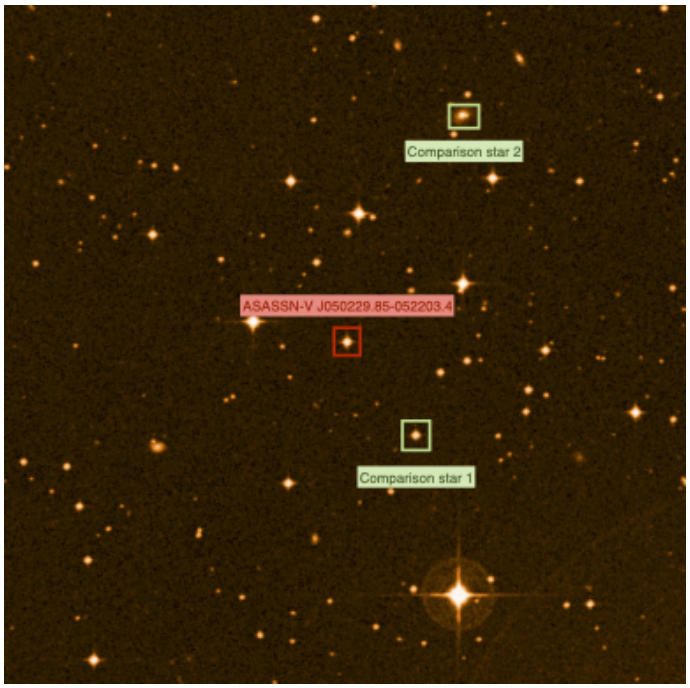

Figure 12: 11x11 arcmin starfield of ASASSN-V. In red, the binary system. In green, the comparison stars chosen (European Southern Observatory, 2025).

2.3 Observation with IAC80 telescope

2.3.1 CAMELOT2

CAMELOT2 camera (*CAmara MEjorada Ligera del Observatorio del Teide* in Spanish) is the primary instrument of the IAC80 telescope, installed in the telescope's Cassegrain focus (IAC, 2024d). This camera operates in the optical wavelength range, featuring a 4096×4112 pixel array with each pixel of 15×15 μm. It provides a scale in the sky of 0.322 arcsec/pixel and a field of view (FOV) of 22×22 arcmin^2.

The CCD has 5 different readout modes that provide different readout velocities and readout noise (RON). We chose Mode 0 for our observations as its readout time and readout noise (RON) offer an optimal balance between adequately sampling the binary phases, and achieving a satisfactory signal-to-noise ratio (SNR) with its gain (defined as the number of electrons required to register a count).

Table 2: Properties of CAMELOT2 when using mode 0 (IAC, 2024a).

Readout speed [kHz]	Readout time [s]	DR [counts]	Recommended flat counts	Gain [e^-/ADU]	RON [e^-]
344 (Attn 0)	13.5	56000	39000	4.23	6.01

The linear response of the detector is crucial, as it determines whether light measurements from celestial objects can be accurately obtained. It is determined by the storing capacity of photoelectrons in each pixel. The criterion for determining the detector's count limit (ADU) is based on the saturation counts of the first channel for each mode. For the mode used in observations, Mode 0, ADU is set at 56000 counts (see Figure 13 and Table 2).

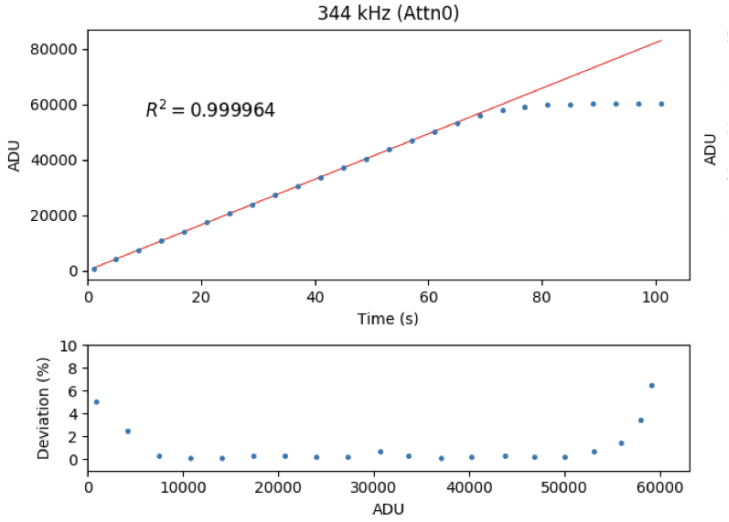

Figure 13: CCD linearity for mode 0 of CAMELOT2. For this mode the dynamic range is 56000 counts (Aguado, 2021).

An important issue with CAMELOT2 is that the filter wheel was recycled when changing the telescope instrument from CAMELOT to CAMELOT2; thus, the filter wheel now produces vignetting in the images (see Figure 14), reducing the usable field to a square of 11.8 × 11.8 arcmin^2 (IAC, 2024a).

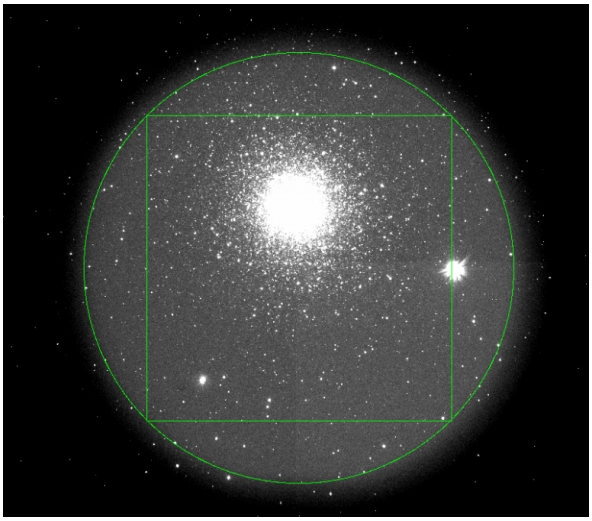

Figure 14: Vignetting of CAMELOT2 field of view. The circle has a field of 16.8 arcmin of diameter and the square has a field of 11.8 x 11.8 arcmin^2 (IAC, 2024a).

2.3.2 Calibration images

Bias

The bias level is an intrinsic variable of the CCD, for all pixels and independent of the filter, as it is generated with a zero-time exposure. It introduces an artificial number of counts to prevent negative values resulting from readout noise.

To measure the level of artificial counts, we took bias images. They show the spatial distribution of these artificial count levels. With the IAC80 telescope, acquiring these calibration frames involves closing

the telescope petals while pointing at the zenith, switching off the dome lights. Each observation night, a total of 21 bias images are collected.

It exists also a region of pixels generated electronically, known as the overscan, which is typically used to monitor temporal variations in the bias level, allowing the bias value to be obtained simultaneously with data acquisition. The overscan captures the temporal fluctuations of the bias. However, CAMELOT2 does not include an overscan region.

Flat-fields

In a CCD, not all pixels have the same quantum efficiency, thus the number of electrons detected per incoming photon varies depending on the wavelength. Also, illumination on the focal plane is not uniform due to the optical system and the presence of dust particles. Flat-field are images of a uniformly illuminated field to correct this effects of artificial light variations.

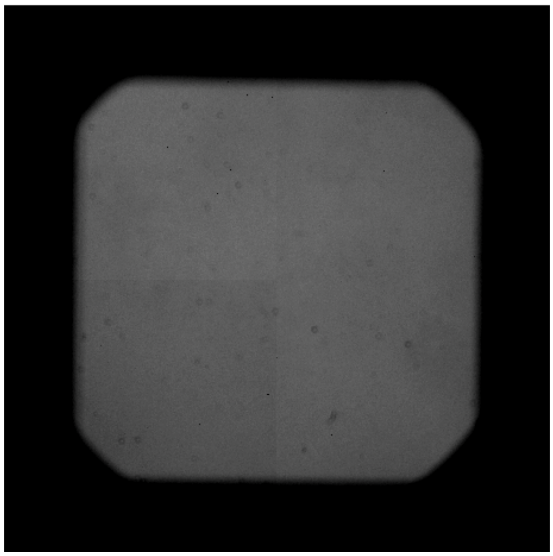

Figure 15: Flat-field image in filter V. Here it can be observed the vignetting of the filter wheel.

Since quantum efficiency varies with wavelength, it is necessary to take flat-field images for each filter used. There are two types of flat-flied images based on how they are acquired: sky flat-fields and dome flat-fields:

- Sky flat-fielde are a type of flat images obtained using a uniformly illuminated section on the sky. Generally, the telescope is pointed 45º above the horizon towards the east, to obtain constant luminosity instead of gradient. However, this type of flat-field image presents several challenges. First, the time available to take this images is limited; during the observation months, twilight lasts less than a hour (30 minutes in this observation run (Agencia Estatal de Meteorología, 2023), which makes difficult to capture enough sky flat-field images for all filters. Second, a completely clear sky is needed, as the presence of cirrus clouds disrupts the uniformity of the light distribution. Finally, it is necessary to move the telescope pointing to prevent stars in the final flat calibration.
- Dome flat-field images are exposures of an artificially illuminated screen inside the telescope dome. For the IAC80 telescope, the telescope should be pointed south, and the dome is adjusted so that the white screen fills the entire FOV of the camera. The screen is illuminated by two lights, one white and one red, adjusted to obtain an appropriate number of accounts. For flat-field images, the limit is set

at 70% of the saturation counts, equivalent to 39000 counts in our observing configuration (Aguado, 2021). Each observation night, we took 11 dome flat-field images per filter (see Figure 15).

2.4 Observation of ASASSN-V J050229.84-052203.4

2.4.1 Auto-guiding

Once bias and flat images were acquired, we entered the ASASSN-V coordinates into the telescope system, first for pointing and then to enable tracking and compensate Earth's rotation. Additionally, we configured the FOVIA auto-guiding. This tool detects minor tracking drifts (noticeable only for exposure times longer than 30 seconds) using an auxiliary camera and a guiding star. The guiding star must be clearly luminous in order to detect the small shifts of the telescope, which are corrected by the guiding system.

At the IAC80 telescope, the auxiliary camera shares the telescope's field of view and must be positioned carefully to avoid interfering with the field of view of CAMELOT2. We used a joystick to search for a suitable guide star, and once this star is located and fixed by the system, the arms of the FOVIA system are retracted to prevent any shadows from appearing on the CCD field.

2.4.2 Observation exposure times

After obtaining bias and flat-field images, poiting the telescope, and configuring the auto-guiding tool, the observation is ready to begin. To determine the appropriate exposure times, we used the pre-calculated exposure times as a reference (IAC, 2024c). Since the detector has a linear respond, we could easily compute the final exposure times based on the counts measured in the test images. We selected the optimal exposure times (see Table 3) such that neither the binary nor the comparison stars would saturate, as well as that there was a good signal considering that the magnitude of the binary would drop in eclipses.

Table 3: Exposure times for ASASSN-V in the IAC80 telescope with the Johnson filters.

Filter	**Filter V**	**Filter R**	**Filter I**
Time [s]	300	300	150

Exposure times were shorten on certain days due to favorable meteorological conditions. Conversely, on some nights, adverse weather resulted in longer exposure times or even impeded the acquisition of high-quality data (see Table 14 in Appendix A.2).

2.5 Image post-processing

2.5.1 Reduction process

When an observation is carried out, the detected signal is influenced by the effects introduced by the instrumentation. To extract accurate information, the data must undergo reduction, meaning that the

object images need to be corrected for bias and flat-field variations. The acquired signal is given by the following equation:

$$S(x, y) = B(x, y) + [I(x, y) \cdot F(x, y) + D(x, y)] \cdot t_{exp} \tag{14}$$

where B is the bias signal, I the corrected signal, F the normalized flat-field signal, D the dark signal (negligible for CAMELOT2, see Figure 16), and t_{exp} the exposure time. Consequently, the corrected pixel value with (x, y) position is determined as follows:

$$I(x, y) = \frac{S(x, y) - B(x, y)}{F(x, y)} \cdot \frac{1}{t_{exp}} \tag{15}$$

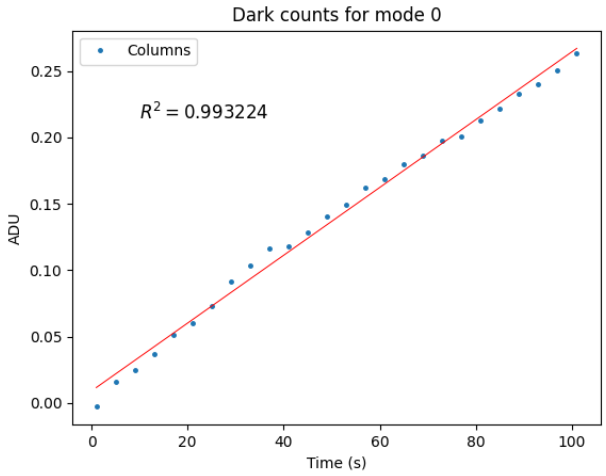

Figure 16: Dark counts for mode 0 of CAMELOT2. The slope of the fit is 0.0255 ADU/s, so dark counts are negligible for CAMELOT2 (IAC, 2024a)

The data reduction process is shown in Figure 17.

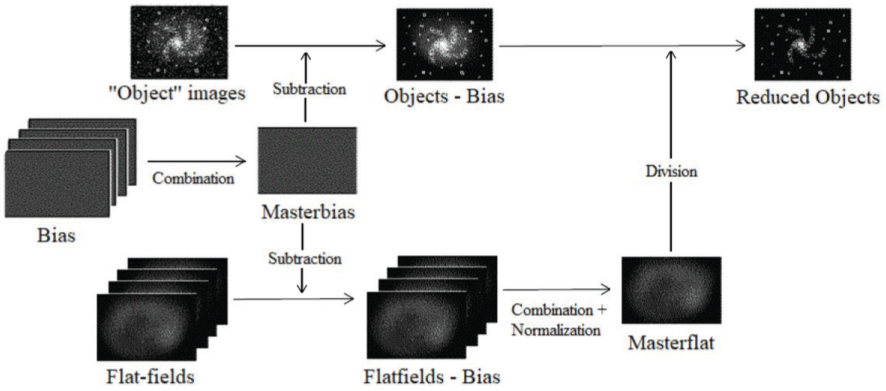

Figure 17: Data reduction process (Galán-Diéguez and Garzón-Heydt, 2021)

PhotoRed

We performed the data reduction process using the script `PhotoRed`, developed by D. Galán-Diéguez. This program uses the `PyRAF` environment, which enables the use of `IRAF` (*Image Reduction and Analysis Facility, NOAO*) functions within `Python`.

Once all the necessary modules and packages are loaded, the next step is to define the parameters needed to run `PhotoRed`. In the console, the following information must be provided. We have to decided if we want `PhotoRed` to use the masterbias image, to extract the bias level. It is also possible to specify if the overscan section is used in the reduction process (this region is defined in the telescope file), and if the user wants to trim the images (this trimming section is also defined in the telescope file). Next, it reads the telescope parameters. The *.json* telescope file contains specifications such as trim and overscan sections, and header structure based on the image type (object, bias, or flat-field). It also provides key values such as gain, readout noise (RON), saturation level, scale, and field of view (FOV) radius.

Once all the parameters are set, the program reads all the files from the specified path and classifies them into three categories: bias, flat-fields, and target images. The flat-field array is then analyzed to identify the filters used during the observation. Additionally, it reads the header parameters from the telescope's *.json* file. Next, the bias list is displayed, including statistics such as mean, minimum, maximum, midpoint, and standard deviation. This allows the user to identify and select any low-quality bias images for exclusion from the reduction process (though the program does not remove them from the directory). The same procedure is applied to the flat-field list.

It creates a support folder at the home directory to avoid issues with file paths, as `IRAF` may fail with lengthy paths. The bias, flat-field, and object images are copied to this folder. Since there are multiple bias and flat-field images, they should be combined into what are known as the masterbias and masterflat, respectively. So, the first step is to combine the bias images to create the masterbias. Thus, the program uses the `imcombine` module to create the masterbias (see Figure 18). Since flat-field images has non-zero exposure time, they must be corrected for bias. Flat-field images are corrected for masterbias and trimmed using the `ccdproc` module, and then it generates the masterflat for each filter using the `flatcombine` module. All the mentioned modules are part of `IRAF.`

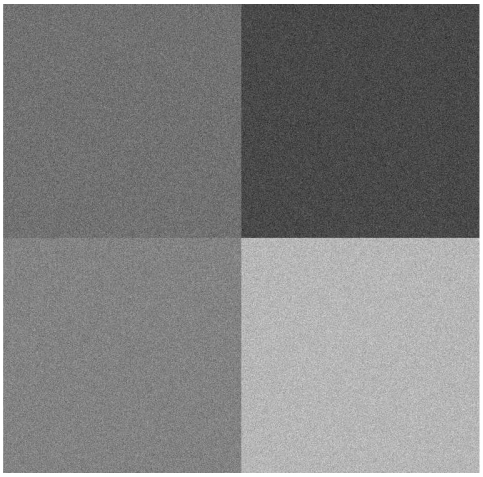

Figure 18: Masterbias. Four distinct levels are detected due to the detector's four readout channels.

Then, `PhotoRed` subtracts the masterbias from the object images, trim them with `ccdproc` and correct them from masterflat for each filter. With this step, the reduction process is finished.

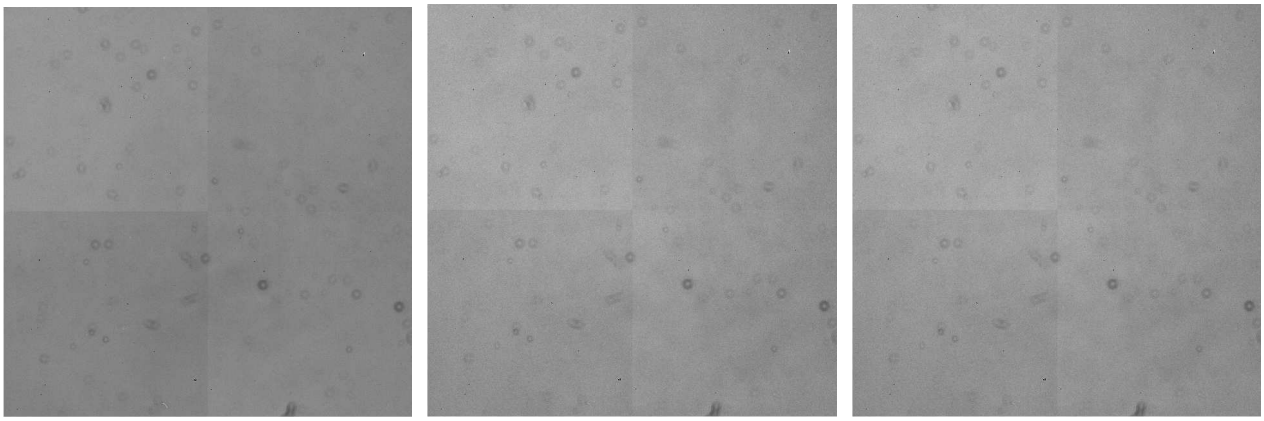

(a) Masterflat filter I (b) Masterflat filter R (c) Masterflat filter V

Figure 19: Masterflats. As the images have not yet been corrected from bias, the four different readout channels remain visible.

Finally, `PhotoRed` saves the processed files (masterbias, masterflats, and reduced object images), displays the masterbias and masterflats in the DS9 viewer, and activates the `imexam` command for value checking. Also, it moves all of these files to a new folder created at the original file path, deletes the support folder, and generates a log file. The log file contains important information about the reduction: bias and flat-field statistics before processing, together with the masterbias and the masterflat statistics, reduction parameters used, etc (see Table 13 in Appendix A.1).

2.5.2 Astrometry process

Although the telescope has been calibrated to compensate the Earth rotation, it is necessary to find out a relationship between celestial coordinates and pixels positions (x, y). To do it, we used `AstroNet` script.

AstroNet

To perform the astrometry process, we used the program `AstroNet`, also developed by D. Galán-Diéguez. Similar to `PhotoRed`, it runs within the `PyRAF` environment. However, in addition to the modules used by `PhotoRed`, it requires the `astroquery.astrometry.net` package from `Python`. In addition, it needs two support files, telescope and CCD parameters.

Additionally, it sets a minimum and maximum star detection threshold of 30 and 300 stars, respectively. Now, the `Starfind` parameters should be defined. A filter detection process must be performed, similar to `PhotoRed`, to categorize images based on their filters. Then, two options are provided depending on whether the FWHM is known. In this case, it was set to 5 for each filter.

At this point, the astrometric alignment begins. It detects the stars and sends the positions to `Astronometry.net`, which returns the transformation equations, saved on the image headers. Once all images have been processed, `AstroNet` generates a log file, marking the completion of the process.

2.6 Differential Photometry

The last step in the data processing before computing the light curve is the photometry. In this case, we performed differential photometry with the script `BinaPhot`, also included in `PHOTOBIN`.

Once all arguments have been defined, it reads the photometric parameters of the telescope and those from the image headers. Additionally, it sets parameters for the `phot` and `starfind` algorithms. This script includes an option to limit the aperture, if needed; ir our case, when obtaining the instrumental magnitudes for the calibration stars (Landolt catalog, Landolt, 2009), we used a fixed aperture of 7 pixels.

Once this setup is completed, the photometry process begins. It starts with star detection within the field, requiring the identification of at least 30 and no more than 200 stars. This detection process can be repeated up to 20 times until it achieves a convergence. Then, it computes the FWMH and the seeing of the image. The coordinates of both the comparison stars and the binary system are transformed from celestial coordinates to *(x, y)* using the astrometry equation from `AstroNet`. Next, the program establishes the local observatory database to compute the epoch, the sidereal time, and the heliocentric Julian date (HJD) for the image. It then reads the airmass from the image header and compute effective airmass for the binary system; as the binary system is close to the comparison stars, the airmass variation is less than one thousandth of a percent. It also determines photometry-related values such as the FWHM of the PSF, the estimated standard deviation of the sky pixels, and the inner radius of the annular sky-fitting region (in units of the DATAPARS scale parameter). To optimize the aperture radius, the program calculates SNR values for the binary system and for the comparison stars, and takes the optimal aperture. The SNR equation is defined as

$$S/N = \frac{N_*}{\sqrt{N_* + n_{pix}(N_S + N_D + \sigma^2_{RON})}} \tag{16}$$

where N_* is the number of photoelectrons produced by the source within the aperture, n_{pix} the number of pixels which form the aperture, N_S the number of electrons per pixel produced by the sky background, N_D the dark current and σ^2_{RON} the readout noise.

To correctly determine the local background variations, the skyring must be close to the source, so the annulus must have a value about 4·FWHM. The dannulus value is determined with the aperture value, fixed such that the sky ring has an area 200 times the area of the aperture. Photometry is then performed on both the binary system and the comparison stars, and the results are checked for errors.

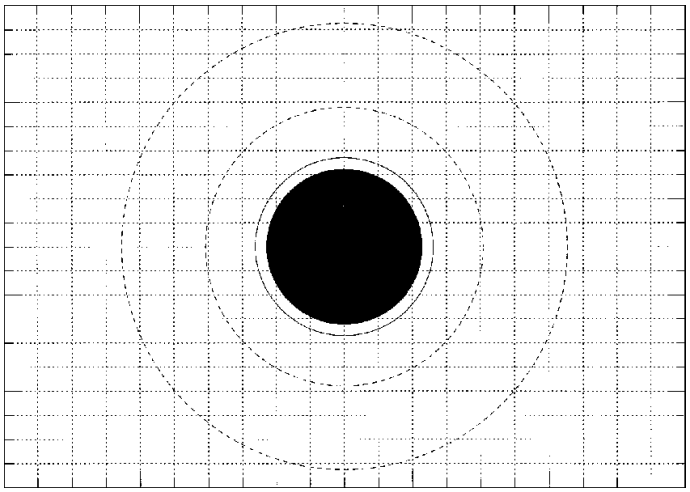

Figure 20: Schematic drawing of a stellar image on a CCD pixel grid. The figure shows the location of the star, the solid line represents the "star" aperture, the inner dashed circle the annulus, and outer dashed circle the dannulus (Howell, 2006).

Differential photometry begins next. `AstroNet` creates three arrays to store the instrumental magnitude differences between components: two arrays hold the difference between the binary system and each of the comparison stars, and one contains the difference between the comparison stars themselves. It also computes the errors in these differential magnitudes using the SNR of the measurements.

Finally, it generates and saves log files in a new folder. One is a CSV file containing important metadata of the photometry process such as the image name, HJD, effective airmass, seeing, and aperture size. Also, the fundamental results of the differential photometry, that is instrumental magnitudes of the binary system and comparison stars, differential magnitudes (with errors). The second log file consists of visual results, including two plots: one showing the differential magnitudes of the binary system relative to each comparison star, and another showing the differential magnitude between the comparison stars. In this last plot, outliers beyond 3σ are highlighted in red. Additional plots show the evolution of the seeing and airmass during the observation (Figure 21). With this, the differential photometry results are fully obtained.

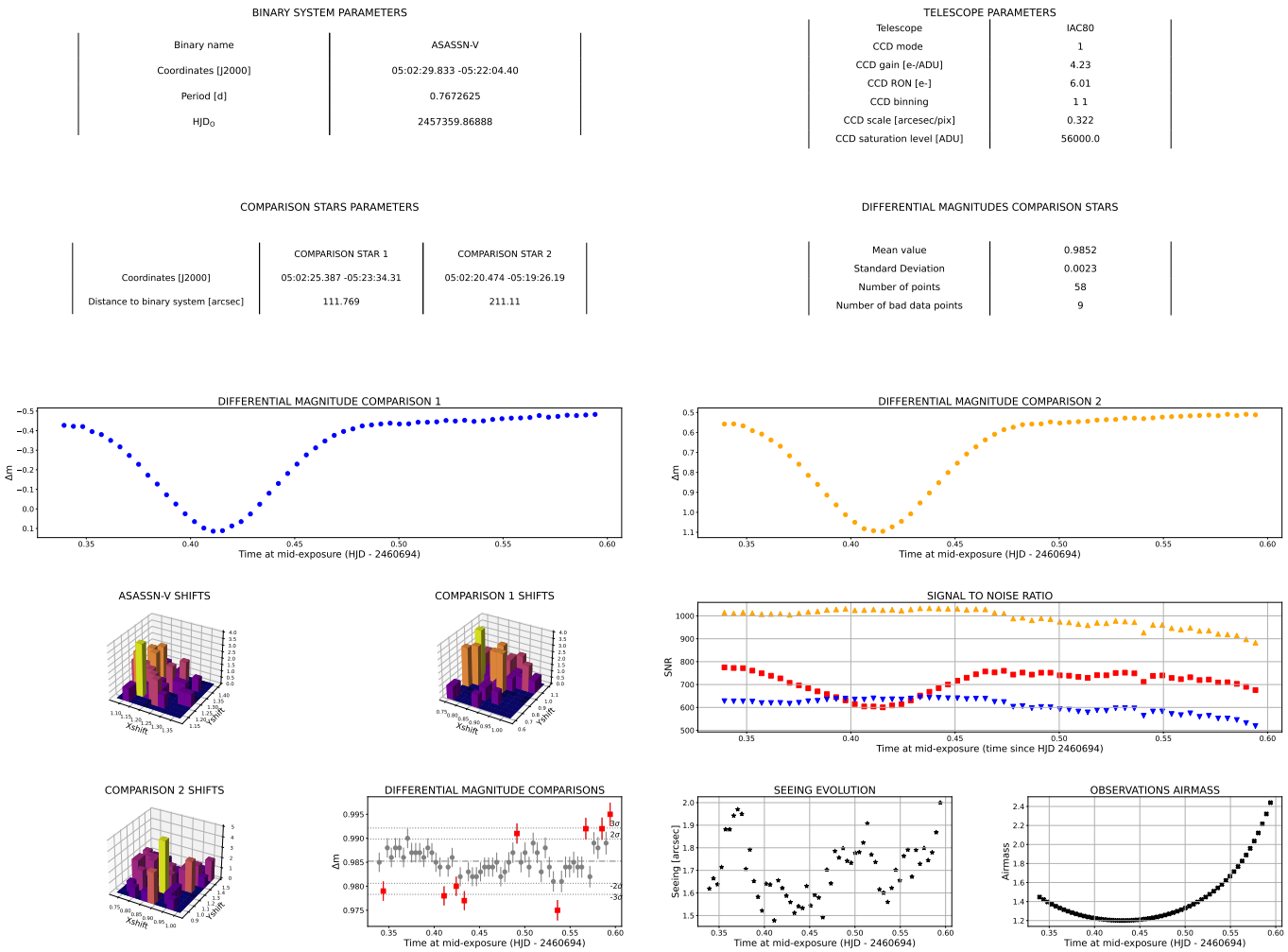

Figure 21: Visual results produced by `BinaPhot` for the night of January 19, using filter V

3 Light curve of the eclipsing binary ASASSN-V J050229.84-052203.4

Resumen: En este capítulo se presenta la curva de luz obtenida para el sistema binario eclipsante ASASSN-V J050229.84-052203.4, como resultado del procesamiento fotométrico de los datos. A partir de su análisis preliminar, se identificaron características relevantes como la forma de los eclipses y ciertas modulaciones fuera de ellos, que ofrecen pistas sobre la geometría y actividad de las componentes estelares del sistema.

Now, we can obtain the light curves of the eclipsing binary ASASSN-V using both the instrumental magnitude and the HJD of each data point (see Figure 22).

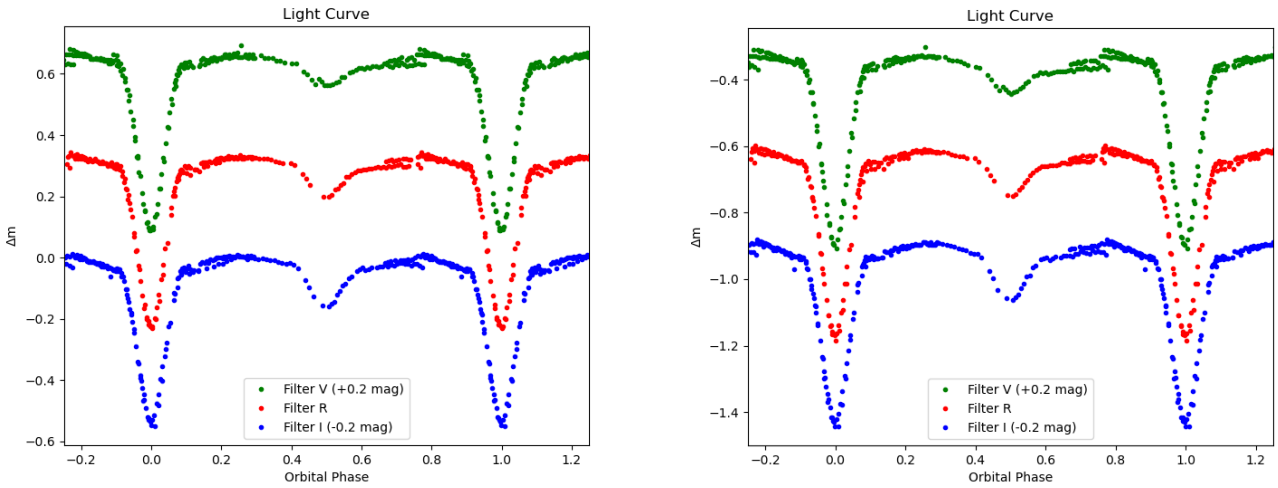

Figure 22: ASASSN-V J050229.84-052203.4 light curves for Johnson V, R and I filters. On the left, the differential magnitude is calculated with comparison star 1. On the right, with comparison star 2. Note: filter V and I have been shifted in order to get a better view.

As observed, the ASASSN-V binary system exhibits partial rather than total eclipses. This means that, from our line of sight on Earth, the secondary star is not entirely obscured during the secondary eclipse, and likewise, the primary star is not fully hidden during the primary eclipse. This occurs because the orbital inclination is not exactly 90º. Also, by the form of the curve in out-of-eclipse phase, it looks like there is magnetic activity that produces spots in the stars. This out-of-eclipse variation is more pronounced in the V filter, which suggests the presence of cold spots.

4 Photometric calibration

Resumen: En este capítulo se describe el proceso de calibración fotométrica realizado a partir de observaciones de campos estándar de Landolt, con el objetivo de determinar las magnitudes calibradas y los índices de color del sistema. Para obtener colores intrínsecos más precisos, se aplicó una corrección por enrojecimiento interestelar utilizando datos de Gaia. A partir de los colores corregidos, se identificó una compatibilidad con un tipo espectral aproximado A7 para la estrella primaria.

To determine an approximation of the spectral types of both components of the binary system ASASSN-V, we performed photometric calibration over the photometric night of January 18, 2025. We observed two Landolt fields, RU149 and PG0942-029 (Figure 23), covering a wide range of airmasses, and using the Johnson V, R and I filters. We selected this two fields because of their number of stars, which permit us calibrated with a lot of different stars with only two fields. This makes the job easier (Table 4).

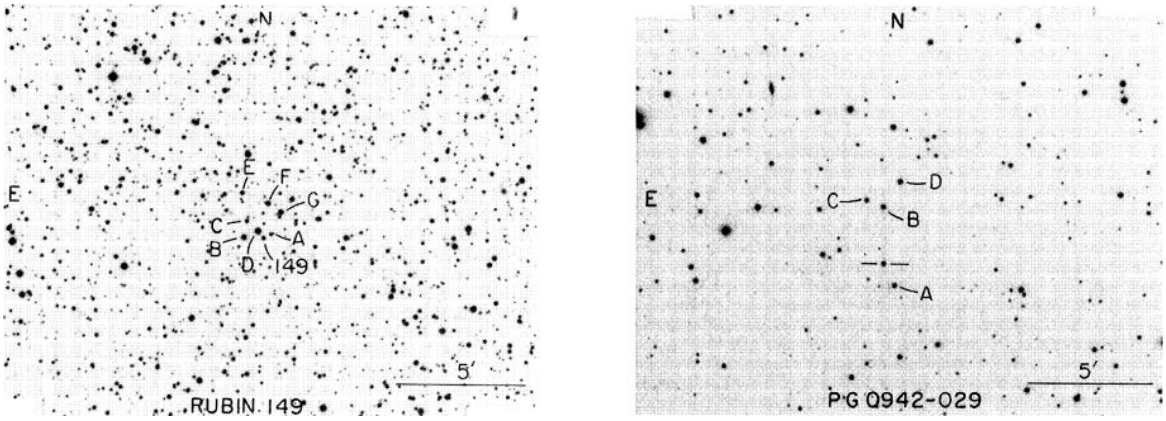

Figure 23: RU149 and PG0942-029 Landolt fields. Right: RU149. Left: PG0942-029

Table 4: Landolt fields observed in the photometric night 2025-01-18

Night	Field	#N stars	#N measurements per filter	Airmass range
2025-01-18	RU149	8	18	1.272-2.209
	PG0942-029	5	22	1.173-2.302

First, we verified that the selected night was photometric. To do this, we used the Bouguer lines for all the standard stars, which represent the relation between the airmass variations and the instrumental magnitude. Figure 24, shows the Bouguer line on the night of January 18, 2025 for some of the calibration stars in Johnson V, R and I filter. Once this verification was completed, we carried out the photometric calibration process.

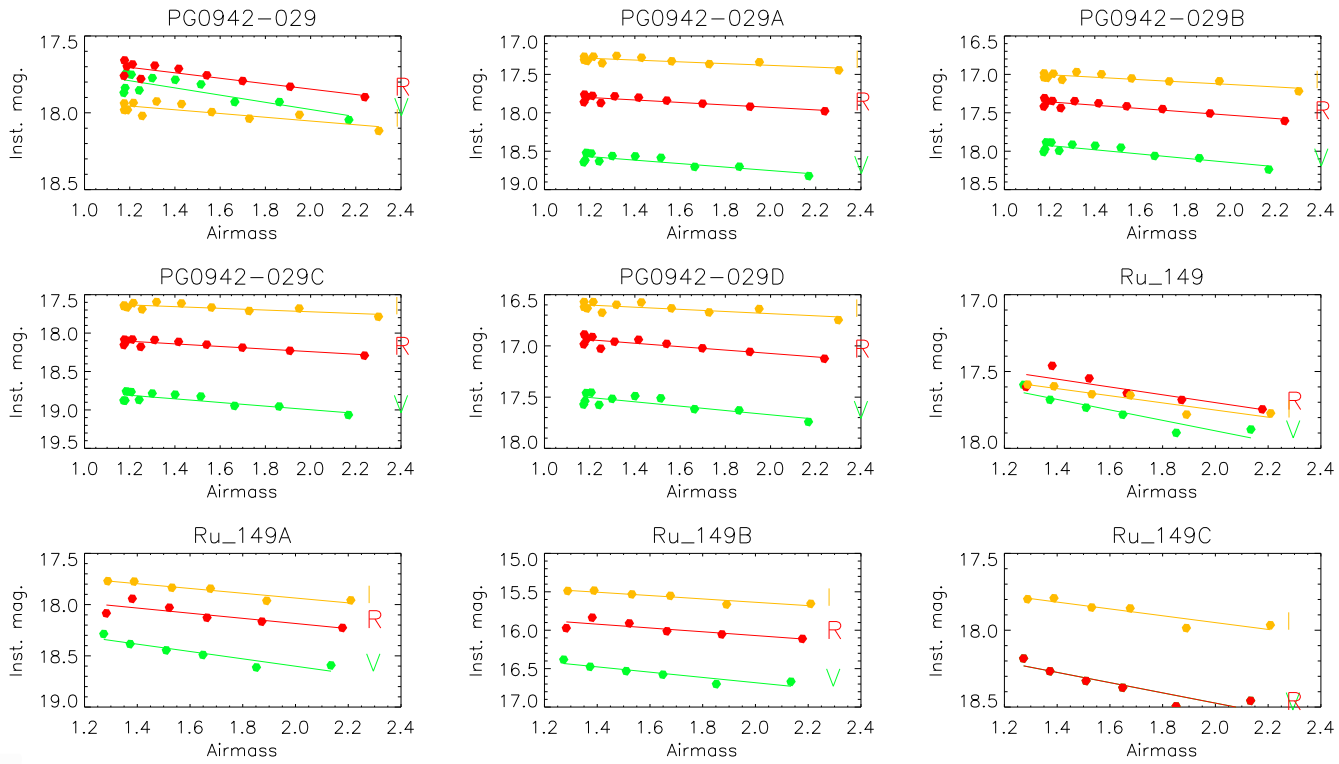

Figure 24: Bouguer graphs for some of the calibration stars

In order to obtain the calibrated magnitudes, we use the following set of equations for each Landolt star:

$$\begin{aligned} V &= m_V^{inst} - a_0 - a_1 X_V - a_2(V-R) - a_3 X_V (V-R) \\ R &= m_R^{inst} - b_0 - b_1 X_R - b_2(R-I) - b_3 X_R (R-I) \\ I &= m_I^{inst} - c_0 - c_1 X_I - c_2(R-I) - c_3 X_I (R-I) \end{aligned} \tag{17}$$

where m^{inst} are the instrumental magnitudes and X the airmass values. So, since we have 13 stars, we have 39 equations but only 12 unknown variables. Thus, we have an overdetermined system. The final calibration parameters will be those that achieve the best fit.

Figure 25 represents calibrated magnitudes versus catalog magnitudes for standard stars for the minimum airmass of the observations. This should be a 1:1 relation because we are comparing the magnitude of the literature with the calibration. In it, the points in filter V and filter I are distributed symmetrically around the line. But, in filter R, all the points are above the line. In small airmasses, observations for filter R has oscillations that could be produced by a cloud or extinction changes. However, if these graphs are made with all the magnitudes calculated for all the airmasses, they are distributed on both sides of the line.

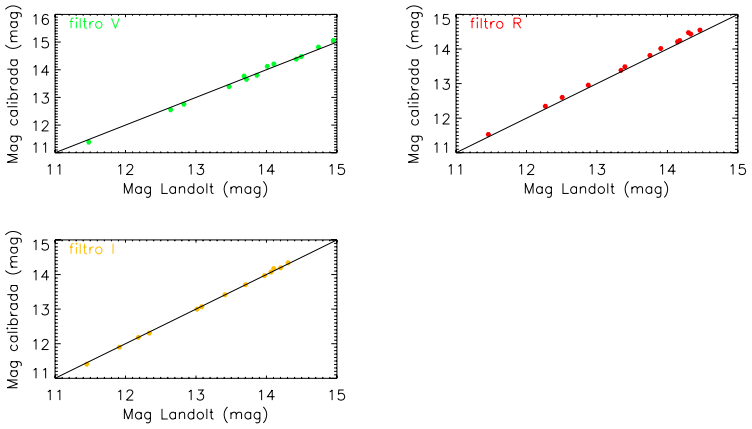

Figure 25: Calibrated magnitude vs catalog magnitude for calibration stars to the minimum airmass of the observations. The line has slope 1.

Table 5: Fit parameter values

Parameter	2025-01-18
a_0	3.4345 ± 0.0021
a_1	0.2804 ± 0.0023
a_2	0.1608 ± 0.0061
a_3	-0.0426 ± 0.0039
b_0	3.3053 ± 0.0025
b_1	0.2248 ± 0.0016
b_2	0.1675 ± 0.0075
b_3	-0.0548 ± 0.0048
c_0	3.3850 ± 0.0043
c_1	0.1758 ± 0.0026
c_2	-0.0164 ± 0.0125
c_3	-0.0344 ± 0.0077

Using the calibration parameters listed in Table 5, which were obtained with an IDL script develovep by Ramón Iglesias-Marzoa, we computed the calibrated magnitudes of the comparison stars (see Table 6).

Table 6: Calibrated magnitudes of the comparison stars for each filter

m_{comp1}			m_{comp2}		
Filter V	Filter R	Filter I	Filter V	Filter R	Filter I
14.054	13.717	13.405	13.051	12.780	12.513

Since the difference between the comparison star and the binary system should be the same for both the instrumental and the calibrated magnitudes (approximately), the calibrated magnitudes of the binary system can be derived accordingly, as shown in Equation 18:

$$\begin{aligned} \Delta m_{inst} &\approx \Delta m_{cal} = m_{comparison} - m_* \\ m_* &\approx m_{comparison} - \Delta m_{inst} \end{aligned} \tag{18}$$

where m are the calibrated magnitudes and Δm_{inst} the instrumental differential magnitude. First, we calibrated the comparison stars and then measure Δm_{inst} in the primary eclipse, secondary eclipse and out-of-eclipse phases (see Table 7) in different nights. Then, we computed the calibrated magnitudes of the binary system ASASSN-V in said different phases using both comparison stars (Table 8). As it was expected, the calibrated magnitudes are approximately the same if they are done with comparison star 1 or comparison star 2.

Table 7: Δm_{instr} for comparison stars for each filter and in different phases

	Δ_m^{comp1}			Δ_m^{comp2}		
Phase	Filter V	Filter R	Filter I	Filter V	Filter R	Filter I
Primary eclipse	-0.107	-0.230	-0.227	-1.097	-1.168	-1.231
Secondary eclipse	0.359	0.199	0.040	-0.645	-0.755	-0.867
Out of eclipse	0.457	0.324	0.201	-0.545	-0.615	-0.695

Table 8: Calibrated magnitudes and color indices of the binary system in different phases using both comparison stars.

With comparison star 1			
Filter	Primary eclipse	Secondary eclipse	Out of eclipse
V	14.161	13.696	13.597
R	13.947	13.518	13.393
I	13.742	13.365	13.205
V-R	0.214	0.178	0.205
V-I	0.419	0.331	0.393
With comparison star 2			
V	14.148	13.696	13.596
R	13.948	13.535	13.396
I	13.743	13.380	13.207
V-R	0.200	0.161	0.201
V-I	0.405	0.316	0.389

With these calibrated magnitudes, we calculate the color indices *V–R* and *V–I*. These values enable the determination of the spectral types of each component of the binary system by comparison with standard main-sequence spectral type tables from Johnson, 1966. Our color indices, it suggests that the spectral type of the primary star is an A7 (Johnson, 1966). However, for the secondary star a conclusion cannot be obtained because the primary star still contributes to the flux, making the secondary star appear brighter than it really is.

Finally, we compared our ASASSN-V calibrated magnitudes with those derived from the Gaia database (Gaia Collaboration, 2020). To do so, we used the following transformation equations (Busso et al., 2022):

$$V = G + 0.02704 - 0.01424(G_{BP} - G_{RP}) + 0.2154(G_{BP} - G_{RP})^2 - 0.01426(G_{BP} - G_{RP})^3 \quad (19)$$

$$R = G + 0.02275 - 0.3961(G_{BP} - G_{RP}) + 0.1243(G_{BP} - G_{RP})^2 + 0.01396(G_{BP} - G_{RP})^3 - 0.003775(G_{BP} - G_{RP})^4 \quad (20)$$

where G and $G_{BP} - G_{RP}$ are Gaia magnitudes. The results obtained are shown in Table 9.

Table 9: V and R magnitudes calculated from Gaia.

	Comparison 1	Comparison 2	ASASSN-V
V	14.262	13.284	13.822
R	13.902	12.968	13.593

4.1 Reddening

Dust is formed by heavy elements synthesized within stars via nuclear fusion. These elements are expelled into space via stellar winds and explosive events, and are subsequently reprocessed in the interstellar medium to form dust grains. Dust scatters and absorbs light, particularly in the ultraviolet to infrared wavelengths, following the dust reddening law. As a result, this effect must be accounted for when performing calibrated photometry.

We calculated the reddening E(B − V) for our binary system using its color excess from Gaia $E(G_{BP} - G_{RP}) = 0.1354$. The relation between them is given by (Paunzen et al., 2024):

$$E(G_{BP} - G_{RP}) = 1.3E(B - V) \tag{21}$$

Thus, for ASASSN-V we have that E(B-V)=0.104. We calculated the excesses E(V − R) and E(V − I) with the extinction standard law (Cardelli et al., 1989):

$$\begin{cases} E(V - R) \approx 0.57E(B - V) \\ E(V - I) \approx 1.25E(B - V) \end{cases} \tag{22}$$

The dereddened colors in primary eclipse, secondary eclipse and out-of-eclipse phases are shown in Table 10.

Table 10: Dereddened colors in different colors for the calibrated magnitudes calculated with comparison star 1.

Color	Primary eclipse	Secondary eclipse	Out of eclipse
V-R	0.153	0.117	0.144
V-I	0.289	0.201	0.263

5 Light curve fitting

Resumen: En este capítulo se presenta el ajuste de la curva de luz del sistema binario mediante el software PHOEBE2, utilizando algoritmos basados en inteligencia artificial (EBAI) y técnicas de optimización (Nelder-Mead) para la estimación de parámetros físicos. Aunque no se aplicaron métodos estadísticos más exigentes, como MCMC, debido a limitaciones computacionales, los resultados obtenidos se validaron mediante el uso complementario del programa BinaRoche, lo que permitió comprobar la coherencia de las soluciones.

5.1 PHOEBE2

PHOEBE (PHysics Of Eclipsing BinariEs) is a modeling code for fitting light and radial velocity curves, which uses triangulation as a surface discretization algorithm (Prša, 2011). The original PHOEBE model was based on the Wilson-Devinney code (Wilson and Devinney, 1971), an the new version PHOEBE2 includes new enhancements, like new physics, and new minimization schemes aiming to fully automate the first steps of solution seeking (Prša et al., 2016).

To work with PHOEBE2, it is necessary three numpy arrays that should contains time of the observation (in our case HJD), fluxes and errors. Since our data is differential magnitudes instead of fluxes, we used that

$$\Delta m = -2.5 \log_{10}(F_{rel}) \tag{23}$$

to transform to fluxes. Also, we provided the passband related to each flux data.

In the first step, PHOEBE2 estimates parameters by a very quick process; we used two different types of estimators, both based on machine learning: EBAI MLP uses a trained artificial neural network, and EBAI KNN uses a k-Nearest Neighbors regressor. Then, PHOEBE2 wroks with optimizing algorithms in order to find the best fit to the curve. This is the most computational and time consuming process because of the computational resources needed. In this work, we used the Nelder-Mead optimization, which tries to minimize the differences between the model light curve and the real one by changing the fitting parameters iteratively and selecting the best solution (Nelder and Mead, 1965). The number of iterations used were 500 per filter, because of lack of time and computational resources.

Finally, an algorithm such as MCMC (Markov Chain Monte Carlo) is typically applied to compute uncertainties. In this work, however, we omitted this step due to limited computational resources and time.

During the fitting process, predetermined values were employed due to the absence of radial velocity curves. Specifically, we adopted fixed values for both the eccentricity and the argument of periastron, set to 0. The temperature of the primary star was estimated from the dereddened V – I color and fixed at 8000 K (Huang et al., 2015). Additionally, we used the orbital period and the epoch computed in Fernández-Rodríguez, 2023. The results of the light curve analysis for each filter are detailed in Table 11, while the fits and their residuals are plotted in Figure 26 for filter V, Figure 27 for filter R, and Figure 28 for filter I.

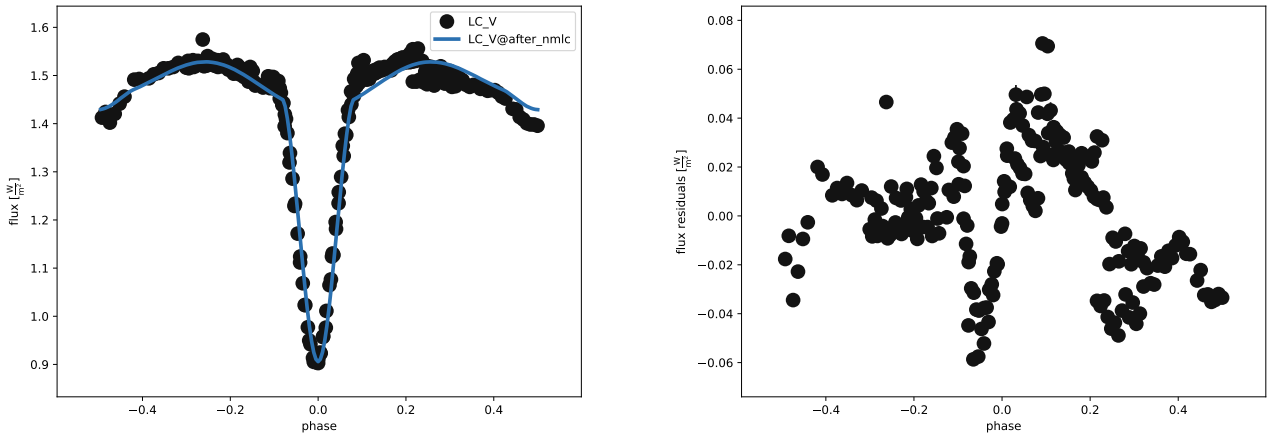

Figure 26: Passband V Nelder-Mead optimization and residuals

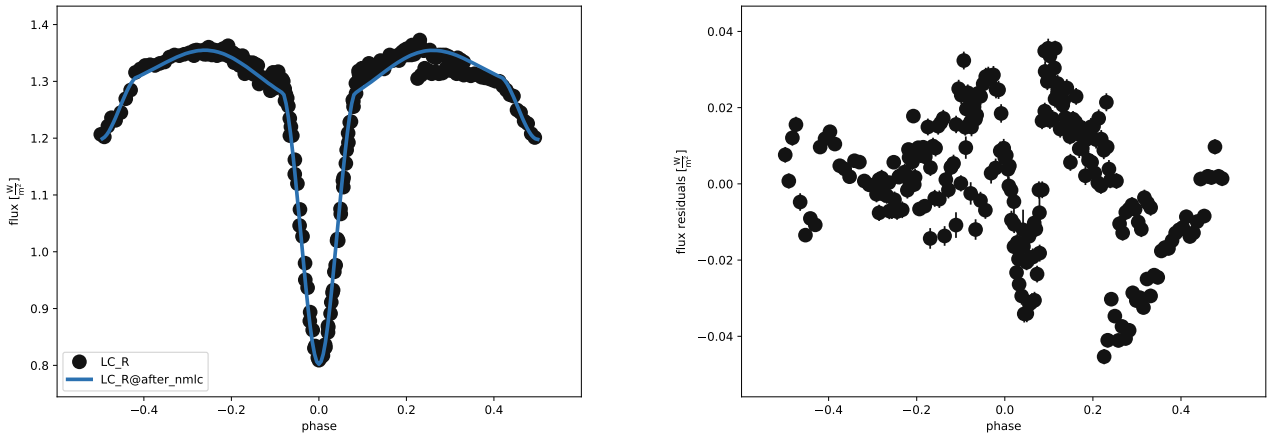

Figure 27: Passband R Nelder-Mead optimization and residuals

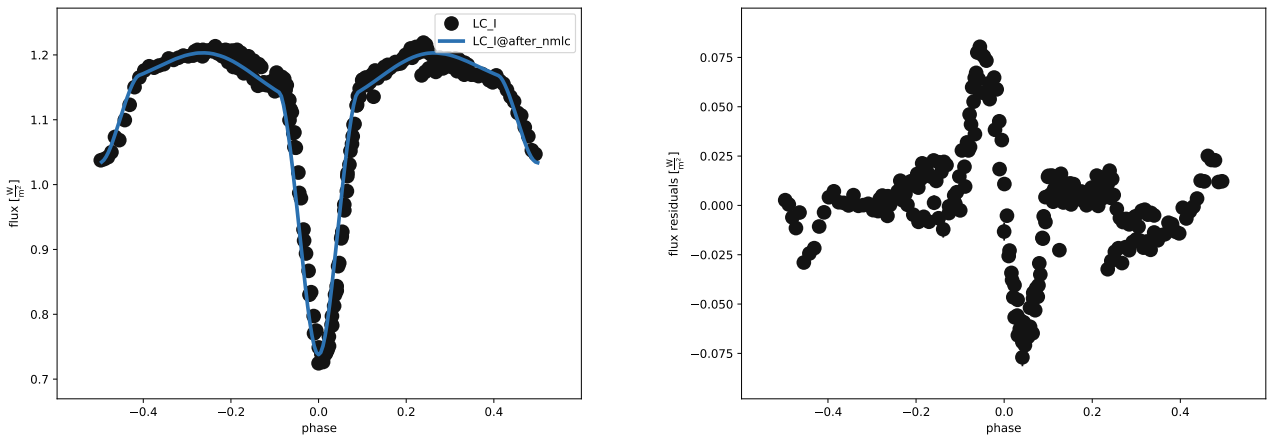

Figure 28: Passband I Nelder-Mead optimization and residuals

Table 11: Fit parameters for ASASSN-V by PHOEBE2

	V	R	I
T_{ratio}	0.5272	0.6552	0.6782
T_1 [K]	8000	8000	8000
T_2 [K]	4218	5241	5425
K	1.0119	0.9171	0.8629
R_1 [$R_\odot$]	1.46	1.79	1.77
R_2 [$R_\odot$]	1.48	1.64	1.52
i [deg]	75.63	76.83	76.76

5.2 BinaRoche

To verify the results of PHOEBE2, we also fitted the ASASSN-V light curves with the program BinaRoche.

The BinaRoche code, developed by Carlos Lázaro (Lazaro et al., 2009), is based on Roche geometry and ATLAS model-atmosphere fluxes. This program simultaneously fits the best parameters of both components of the binary system using light curves in all filters. As initial values, the mass of the primary component was used, calculated to be consistent with the distance provided by Gaia (d = 1298 pc), and it was assumed that the binary system has solar metallicity. The results obtained are given in Table 12 and the fits are shown in Figure 29.

The results obtained from both codes are consistent. Based on these results, the spectral type of the primary component is compatible with an A7 V star, while the parameters derived for the secondary correspond to a K2–K5 V spectral type star.

Table 12: Best fit parameters for ASASSN-V by BinaRoche

T_{ratio}	0.595
T_1 [K]	8000
T_2 [K]	4760
k	0.8861
R_1 [$R_\odot$]	1.42
R_2 [$R_\odot$]	1.25
q	0.3698
M_1 [$M_\odot$]	1.50
M_2 [$M_\odot$]	0.5547
L_1 [$L_\odot$]	7.15
L_2 [$L_\odot$]	0.70
i [deg]	80.76

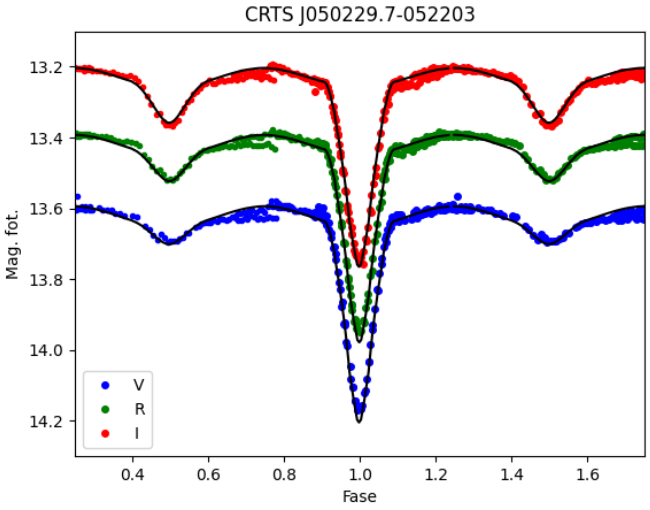

Figure 29: BinaRoche fitting of ASASSN-V light curves in the V, R, and I filters

6 Conclusions and future work

Resumen: Este capítulo resume los logros del estudio, destacando la obtención de curvas de luz bien muestreadas del sistema binario eclipsante ASASSN-V en los filtros Johnson V, R e I. Se utilizaron los programas `PHOEBE2` y `BinaRoche` para ajustar las curvas y derivar parámetros físicos, y se corrigió por el enrojecimiento interestelar, estimando una temperatura de 8000 K para la estrella primaria. El análisis reveló actividad estelar, posiblemente asociada a manchas frías en la secundaria, especialmente evidentes en el filtro V. Se concluye que la estrella primaria es de tipo A7 V, mientras que la secundaria estaría entre K2 V y K5 V. Se propone como trabajo futuro obtener espectros que permitan confirmar las clasificaciones y caracterizar la actividad magnética mediante líneas de emisión como H alpha y el triplete de CaII.

In this study, we successfully obtained well-sampled light curves for the eclipsing binary ASASSN-V J050229.84-052203.4 using Johnson V, R, and I filters. To achieve this, we submitted an observing proposal to the internal Time Allocation Committee (CAT) of the Instituto de Astrofísica de Canarias (IAC). Prior to submission, we identified suitable nights that would ensure adequate coverage of the orbital phases. On-site observations were conducted using the IAC80 telescope and the CAMELOT2 camera, allowing us to gain practical experience in operating the telescope and its associated instrumentation. We learn how to use the `PhotoRed`, `AstroNet`, and `BinaPhot` scripts to process the photometric images and extract the light curves in differential magnitudes.

The light curves of ASASSN-V J050229.84-052203.4 exhibit indications of stellar activity, evidenced by a brightness variation during the quadrature preceding the secondary eclipse. It is likely that the secondary star, considering its spectral type, is responsible for this activity. The out-of-eclipse variation is more pronounced in the V filter compared to R and I, suggesting the presence of cold spots. For further study of these spots, we plan to compare our results with future observations.

To classify the binary's components, we performed photometric calibration on one observing night, obtaining ASASSN-V J050229.84-052203.4 colors, $(V - R)$ and $(V - I)$. We also investigated its interstellar reddening, E(B–V), which was determined to be 0.0723, enabling us to estimate the temperature of the primary to be approximately 8000 K.

The analysis of the light curves, conducted using two different programs, `PHOEBE2` and `BinaRoche`, suggests the primary star is of spectral type A7V, while the secondary ranges between K2V and K5V. To affirm these classifications, spectroscopic observations are required to obtain radial velocity curves and accurately determine the masses of both components. By comparing the binary's spectrum with a spectral library, the primary star can be classified. Subtracting its spectrum, we can estimate the spectral type of the secondary. By studying the ratio of excess emission in the H alpha and H beta lines, as well as in the CaII infrared triplet in the secondary's spectrum, we aim to identify the type of plage activity or prominences present in the system.

References

Agencia Estatal de Meteorología (2023). *Calendario Meteorológico 2024: Información meteorológica y climatológica de España*. NIPO (versión electrónica): 666-23-007-X; NIPO (versión impresa): 666-20-022-2; ISSN: 0213-3849; Depósito legal: M-34484-2023. DOI: 10.31978/666-23-007-X. URL: https://cpage.mpr.gob.es/.

Aguado, Alberto Madrigal (2021). "Caracterización de la cámara CAMELOT2". In: URL: http://riull.ull.es/xmlui/handle/915/23402.

Alonzo-Carrillo, Carlos (2015). *Fantasía y Realidad: Sorprendentes revelaciones*. Palibrio.

British Astronomical Association, Variable Star Section (2011). *Eclipsing Binary Observing Guide*. Accessed: 2025-06-05. URL: https://britastro.org/vss/EBHandbook11.pdf.

Busso, G., C. Cacciari, M. Bellazzini, J. M. Carrasco, F. De Angeli, D. W. Evans, C. Fabricius, P. Montegriffo, E. Pancino, M. Rainer, and N. Sanna (June 2022). *Gaia DR3 documentation Chapter 5: Photometric data*. Gaia DR3 documentation, European Space Agency; Gaia Data Processing and Analysis Consortium.

Cardelli, Jason A., Geoffrey C. Clayton, and John S. Mathis (Oct. 1989). "The Relationship between Infrared, Optical, and Ultraviolet Extinction". In: ApJ 345, p. 245. DOI: 10.1086/167900.

Chen, Yitang (July 2024). "Eclipsing binaries and related photometry". In: *Theoretical and Natural Science* 43, pp. 196–204. DOI: 10.54254/2753-8818/43/20240846.

Christian, Carol and Jean-René Roy (2017). "Stars and Stellar Systems". In: *A Question and Answer Guide to Astronomy*. Cambridge University Press, 75–128.

Drake, A. J. et al. (July 2014). "The Catalina Surveys Periodic Variable Star Catalog". In: ApJS 213.1, 9, p. 9. DOI: 10.1088/0067-0049/213/1/9. arXiv: 1405.4290 [astro-ph.SR].

European Southern Observatory (2025). *ESO Archive: Digitized Sky Survey (DSS)*. URL: https://archive.eso.org/dss/dss.

Fernández-Rodríguez, Gareb Enoc (2023). "Determination of the physical parameters of eclipsing binary star systems ASASSN-VJ050229.84-052203.4 and CRTSJ041918.8-071807". In: URL: http://riull.ull.es/xmlui/handle/915/33699.

Gaia Collaboration (Nov. 2020). *VizieR Online Data Catalog: Gaia EDR3 (Gaia Collaboration, 2020)*. VizieR On-line Data Catalog: I/350. Originally published in: 2021A&A...649A...1G. DOI: 10.26093/cds/vizier.1350.

Galán-Diéguez, Daniel and J P Garzón-Heydt (2021). *Photometric observations of eclipsing binary star systems*. Tech. rep.

Hernández, Ayoze Álvarez, Manuel Ángel Pérez-Torres, and Pablo Rodríguez-Gil (2024). *Testing white dwarf X-ray masses in magnetic cataclysmic variables with dynamical studies*. Tech. rep.

Howell, Steve B. (2006). *Handbook of CCD Astronomy*. 2nd ed. Cambridge Observing Handbooks for Research Astronomers. Cambridge University Press.

Huang, Y., X.-W. Liu, H.-B. Yuan, M.-S. Xiang, B.-Q. Chen, and H.-W. Zhang (Oct. 2015). "Empirical metallicity-dependent calibrations of effective temperature against colours for dwarfs and giants based on interferometric data". In: *Monthly Notices of the Royal Astronomical Society* 454.3, pp. 2863–2889. ISSN: 0035-8711. DOI: 10.1093/mnras/stv1991. eprint: https://academic.oup.com/mnras/article-pdf/454/3/2863/4024019/stv1991.pdf. URL: https://doi.org/10.1093/mnras/stv1991.

IAC (2024a). *CAMELOT2*. URL: https://research.iac.es/OOCC/iac-

managed - telescopes / iac80 / camelot2-2/.

IAC (2024b). *CAMELOT2 SNR calculator*. URL: https://research.iac.es/OOCC/iac-managed-telescopes/iac80/camelot/camelot-snr-calculator/.

— (2024c). *CAMELOT2 SNR calculator*. URL: https://research.iac.es/OOCC/iac-managed-telescopes/iac80/camelot/camelot-snr-calculator/.

— (2024d). *IAC80 Telescope*. URL: https://research.iac.es/OOCC/iac-managed-telescopes/iac80/.

Jayasinghe, T, C S Kochanek, K Z Stanek, B J Shappee, T W-S Holoien, Toda A Thompson, J L Prieto, Subo Dong, M Pawlak, J V Shields, G Pojmanski, S Otero, C A Britt, and D Will (Apr. 2018). "The ASAS-SN catalogue of variable stars I: The Serendipitous Survey". In: *Monthly Notices of the Royal Astronomical Society* 477.3, pp. 3145–3163. ISSN: 0035-8711. DOI: 10.1093/mnras/sty838. eprint: https://academic.oup.com/mnras/article-pdf/477/3/3145/24803083/sty838.pdf. URL: https://doi.org/10.1093/mnras/sty838.

Johnson, Harold L. (Jan. 1966). "Astronomical Measurements in the Infrared". In: ARA&A 4, p. 193. DOI: 10.1146/annurev.aa.04.090166.001205.

Landolt, Arlo U. (2009). "UBVRI Photometric Standard Stars Around the Celestial Equator: Updates and Additions". In: *The Astronomical Journal* 137, pp. 4186–4269. DOI: 10.1088/0004-6256/137/5/4186. URL: https://ui.adsabs.harvard.edu/abs/2009AJ....137.4186L.

Lazaro, C., M. J. Arevalo, and J. M. Almenara (Aug. 2009). "Absolute parameters of the Algol binary Z Vul". In: New A 14.6, pp. 528–538. DOI: 10.1016/j.newast.2009.01.010.

Martínez-País, Ignacio González (2003). *Introducción a la Mecánica Celeste: formulación newtoniano*, pp. 113–139. ISBN: 84-7756-562-6.

Marullo, Sara, Alessandro Marchini, Lorenzo Franco, Riccardo Papini, and Fabio Salvaggio (Dec. 2017). "Preliminary Modeling of the Eclipsing Binary Star GSC 05765-01271". In: *Journal of American Association of Variable Star Observer* 45, pp. 69–72.

Nelder, J. A. and R. Mead (Jan. 1965). "A Simplex Method for Function Minimization". In: *The Computer Journal* 7.4, pp. 308–313. ISSN: 0010-4620. DOI: 10.1093/comjnl/7.4.308. eprint: https://academic.oup.com/comjnl/article-pdf/7/4/308/1013182/7-4-308.pdf. URL: https://doi.org/10.1093/comjnl/7.4.308.

Paunzen, Ernst, Martin Netopil, Michal Prišegen, and Nikola Faltová (2024). "An all-sky catalogue of stellar reddening values". In: *Astronomy & Astrophysics* 689, A270. DOI: 10.1051/0004-6361/202347768. URL: https://doi.org/10.1051/0004-6361/202347768.

Perryman, Michael (2018). *The Exoplanet Handbook*. 2nd. Cambridge, UK: Cambridge University Press. ISBN: 978-1-108-41977-2.

Prša, A., K. E. Conroy, M. Horvat, H. Pablo, A. Kochoska, S. Bloemen, J. Giammarco, K. M. Hambleton, and P. Degroote (Dec. 2016). "Physics Of Eclipsing Binaries. II. Toward the Increased Model Fidelity". In: ApJS 227.2, 29, p. 29. DOI: 10.3847/1538-4365/227/2/29. arXiv: 1609.08135 [astro-ph.SR].

Prša, Andrej (2011). *PHOEBE Scientific Reference*. Tech. rep.

Southworth, J. (May 2012). "Eclipsing Binary Stars: the Royal Road to Stellar Astrophysics". In: *Orbital Couples: Pas de Deux in the Solar System and the Milky Way*. Ed. by F. Arenou and D. Hestroffer, pp. 51–58. DOI: 10.48550/arXiv.1201.1388. arXiv: 1201.1388 [astro-ph.SR].

Taff, Laurence G. (1985). *Celestial Mechanics: A computational guide for the practitioner*, pp. 486–489. ISBN: 0-471-89316-1.

Tawalbeh, Yamam and Mashhoor Al-Wardat (May 2018). "Modified Orbital Elements of The Close Visual Binary Systems Hip11352, Hip70973, and Hip72479". PhD thesis.

Terrell, Dirk (Apr. 2001). "Eclipsing Binary Stars: Past, Present, and Future". In: *Journal of the American Association of Variable Star Observers (JAAVSO)*.

Vives, Teodoro (2003). *Estrellas Binarias*. Recuperado el 27 de octubre de 2017. URL: http://www.portalciencia.net/vives1/vives1.html.

Wilson, Robert E. and Edward J. Devinney (June 1971). "Realization of Accurate Close-Binary Light Curves: Application to MR Cygni". In: ApJ 166, p. 605. DOI: 10.1086/150986.

Yang, Y.-G and Jianyan Wei (Dec. 2008). "Evolutionary Status of RV Trianguli and its Related Algol-Type Binaries". In: *The Astronomical Journal* 137, p. 226. DOI: 10.1088/0004-6256/137/1/226.

A Tables

A.1 PhotoRed results

Table 13: Results of the data reduction

Observation night	No. Bias	Flat-fields				Masterbias		Masterflat (Sta. Dev)		
		ADU (mean)	No. V	No. R	No. I	Mean	Sta. Dev.	V	R	I
01/11/2024	21	34500	11	11	11	497.9	0.89	0.014	0.013	0.010
02/11/2024	21	34000	11	11	11	498.0	0.92	0.014	0.013	0.011
15/11/2024	21	37500	11	11	11	498.2	0.89	0.015	0.013	0.011
20/11/2024	21	39000	11	11	11	498.1	0.87	0.016	0.013	0.011
21/11/2024	21	39000	11	11	11	498.2	0.88	0.015	0.013	0.011
28/11/2024	21	38000	11	11	11	498.0	0.92	0.015	0.013	0.011
29/11/2024	21	38500	11	11	11	497.8	0.87	0.015	0.013	0.010
09/12/2025	21	38000	11	11	11	498.3	0.90	0.015	0.013	0.010
10/12/2024	21	39000	11	11	11	498.4	0.90	0.016	0.013	0.011
11/12/2024	21	39000	11	11	11	498.4	0.93	0.016	0.013	0.011
12/12/2024	21	38500	11	11	11	498.4	0.92	0.015	0.013	0.011
15/01/2025	21	39000	11	11	11	498.0	0.86	0.015	0.013	0.011
17/01/2025	21	37500	11	11	11	498.4	0.93	0.015	0.013	0.011
18/01/2025	21	37000	11	11	11	498.3	0.89	0.015	0.013	0.011
24/01/2025	21	38500	11	11	11	498.3	0.89	0.015	0.013	0.011
25/01/2025	21	39000	11	11	11	498.2	0.88	0.015	0.013	0.011
29/01/2025	21	38000	11	11	11	498.1	0.87	0.016	0.013	0.011
30/01/2025	21	39000	11	11	11	498.3	0.93	0.016	0.013	0.011

A.2 Observation nights details

Table 14: Details of the observation nights

Observation night	Observation time [UT]		Used data	Comments
	Start	End		
01/11/2024	00:17	06:35	✗	- Disconnection of FOVIA because of the presence of a cirrus over the guiding star.
02/11/2024	00:11	06:26	✓	- Centering of the telescope before starting observation.
15/11/2024	23:20	04:43	✗	- Bad weather conditions: 1.5 hours of observation lost at the end of the night.
20/11/2024	-	-	✗	- Bad weather conditions: observation canceled.
21/11/2024	03:04	06:14	✗	- Bad weather conditions: 4 hours of observation lost at the beginning of the night.
28/11/2024	22:14	05:11	✗	- Bad seeing during the night.
29/11/2024	22:47	05:21	✗	- Presence of satellite passage in the images.
09/12/2025	21:47	05:03	✗	- Bad seeing during the night.
10/12/2024	01:02	04:35	✗	- Bad weather conditions: 2 hours of observation lost at the beginning of the night.
11/12/2024	21:53	04:50	✗	- Bad seeing during the night.
12/12/2024	21:29	01:35	✗	- Bad weather conditions: 2 hours of observation lost at the end of the night.
15/01/2025	22:57	02:38	✗	- Bad weather conditions: 3 hours of observation lost at the beginning of the night.
17/01/2025	21:28	02:10	✓	- Observation macro reconfigured due to good weather: exposure times changed.
18/01/2025	19:47	02:09	✓	- Photometric night.
24/01/2025	20:39	01:37	✗	- Bad weather conditions: 1 hour os observation lost at the beginning of the night.
25/01/2025	19:33	01:36	✓	- Observation macro reconfigured due to good weather conditions: exposure times changed.
29/01/2025	19:38	01:16	✓	- Observation macro reconfigured due to good weather conditions: exposure times changed.
30/01/2025	19:45	01:00	✗	- Bad seeing during the night.